An Analog Light Scattering Experiment of Hexagonal Icelike Particles. Part II: Experimental and Theoretical Results

BRIAN BARKEY, K. N. LIOU,* AND YOSHIHIDE TAKANO*

Department of Meteorology/CARSS, University of Utah, Salt Lake City, Utah

WERNER GELLERMAN AND PIERRE SOKOLSKY

Department of Physics, University of Utah, Salt Lake City, Utah

(Manuscript received 13 June 1997, in final form 30 April 1998)

ABSTRACT

The scattering properties of hexagonal icelike crystals as measured in the analog manner by the experimental apparatus described in Part I are presented. The crystals are made out of sodium fluoride (NaF), which has an index of refraction similar to that of water ice. The experimentally determined light intensities scattered from fixed and integrated random orientations of a NaF hexagonal crystal, oriented to produce a two-dimensional scattering profile, compares favorably to the expectations derived from geometric ray tracing methods. Also, the three-dimensional scattering properties of a simulated NaF Parry column, a NaF crystal aggregate, and a NaF plate with a rough surface are compared to results computed from the geometric ray tracing approach. From these comparisons the authors conclude that within the experimental measurement uncertainties and to the degree in which the NaF crystal models approach the geometric and optical ideal, the geometric ray tracing approach is an excellent method to determine the single-scattering properties of hexagonal ice crystals of various shapes in the geometric optics domain.

1. Introduction

Light scattering by hexagonal ice crystals whose sizes are much larger than the incident wavelength can be solved by the geometric optics approach. In this approach, a light beam may be thought of as consisting of a bundle of separate rays that hit the particle and that each ray will then undergo reflection and refraction locally and will pursue its own path along a straight line. The geometric ray tracing method is exact when the size parameter, defined as the ratio of the effective dimension to the incident wavelength, approaches infinity and when the ice crystal is composed of perfectly smooth surfaces. Geometric ray tracing has been used to identify the optical phenomena occurring in the atmosphere (see, e.g., Greenler 1980; Takano and Liou 1990). More recently, scattering properties of more complex ice crystal shapes have also been determined by the geometric ray tracing method (Takano and Liou 1995; Macke at al. 1996). Imperfect ice crystal surfaces can also be accounted for by geometric ray tracing based on a stochastic perturbation method (Yang and Liou 1997).

Although the exact Mie theory for the scattering of spherical water droplets has been verified by experiments carried out by numerous researchers (see, e.g., Sassen and Liou 1979), there is no experiment in the optical region that has been developed to cross check the geometric optics approximation for the calculations of light scattering by hexagonal ice crystals of various shapes and surface imperfections. In Part I, we pointed out that desirable ice crystal shapes and sizes are extremely difficult to generate in a cold chamber for a sufficient time period in association with light scattering experiments. For this reason and for the reason that the success of a light scattering experiment is controlled by the laboratory ice microphysics uncertainties, we determined that it is best to pursue a detailed analog investigation of the scattering properties of hexagonal icelike particles. After considerable searching of the available materials, we found that sodium fluoride (NaF) has optical properties very close to that of ice in the visible wavelength. Because of the physical site limitations, our measurements are made at very large size parameters of about 10 000. The assumption of geometric optics allows us to apply these results to smaller size param-

* Current affiliation: Department of Atmospheric Sciences, University of California, Los Angeles, Los Angeles, California.

Corresponding author address: Dr. Brian Barkey, 201 JFB, Department of Physics, University of Utah, Salt Lake City, UT 84112. E-mail: barkey@mail.physics.utah.edu

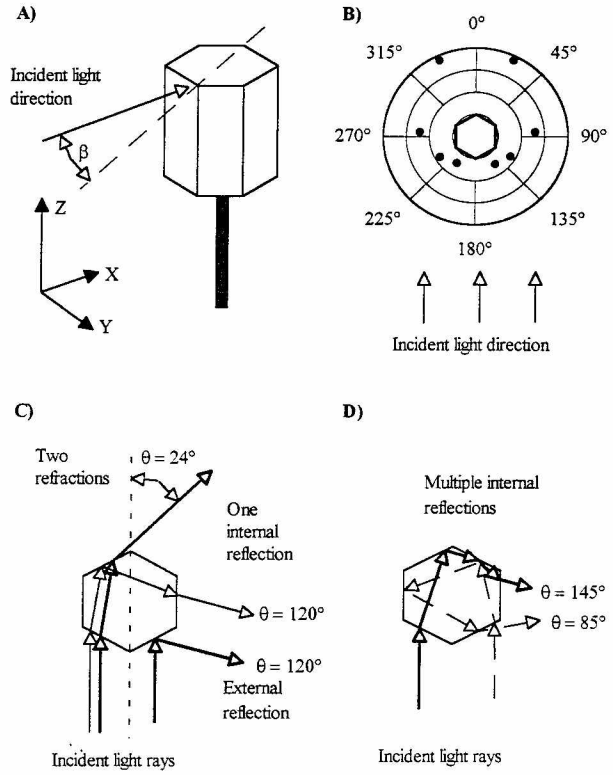

FIG. 1. (a) The orientation of the NaF hexagonal crystal used to produce a 2D scattering pattern showing the crystal orientation angle β. (b) Theoretically derived scattering pattern produced by a 2D NaF hexagon oriented at $\beta = 0°$ as shown on a polar diagram with logarithmic radial scale. (c) and (d) Illustrations of the ray tracing method of predicting scattering properties.

eters (about 100) consistent with the interaction of visible light with natural ice crystals.

This paper presents the phase function results of light scattered from several hexagonal crystals, including columns, plates, aggregates, and crystals with rough surfaces, made out of NaF. The apparatus described by Barkey et al. (1998), henceforth designated as Part I, is used to make these measurements. A description of the NaF icelike particles is provided and then the experimentally measured single scattering results of the simple NaF hexagonal crystal oriented to produce a two-dimensional (2D) scattering pattern, both fixed and integrated across simulated random positions, is compared to theoretical expectations. The experimentally measured light scattered into three dimensions (3D) by an NaF hexagon oriented to simulate the Parry column orientation, an aggregate crystal constructed from several NaF crystals and from an NaF plate with rough surfaces, is compared to theory.

2. 2D NaF hexagon scattering experiments

a. *General consideration for measuring the scattering properties of crystal*

Sodium fluoride powder with a purity of over 99.9% was used to grow a single crystal using the standard Czochralski method and then cut into the hexagonal column shape with a diameter of 5.25 mm ± 0.05 mm and a length of 11 mm. The faces were polished to a smooth finish with 0.25-μm MetadiII polishing compound. This material has an index of refraction equal to 1.325 at the helium neon laser wavelength (0.633 μm), which is very near to that of ice (1.3085 at a wavelength of 0.63 μm) and both have minimal absorption. However, unlike ice, NaF has a face-centered cubic crystalline structure and is not birefringent.

The rectangular faces are referred to as the hexagon sides while the hexagonal end faces are designated as the hexagonal faces. Due to the manual fabrication process, the crystals approach but do not attain geometrical or optical perfection. The vertices or intersection of the side faces are very sharp; a visual estimate of the width of each intersection is 0.1–0.3 mm. The measured angles between the hexagon sides, which should ideally be 120°, vary from 119.3° to 121.3°. Optical measurements showed that the hexagon faces have radii of curvatures that vary from 100 to 140 mm and opposite faces deviate from being parallel by an amount of about 0.3°–1.5°. Visual inspection of the crystal surface revealed small pits and residual scratches that could not be polished out.

To get a quantitative measure of the optical quality of the crystal surfaces, the intensity of light that is externally and internally reflected from opposing and parallel side faces of the hexagon was measured. The measured intensity of reflected light was less than the expected by 0% to −12% for external reflection and −4% to −25% for internal reflection and, visually, the scattered light that undergoes multiple internal reflections is not as sharply defined as that due to direct reflection. We believed that the internally reflected light intensity is affected more strongly because it interacts with more NaF–air interfaces. Finally, to get an idea of the affect that the NaF surfaces have on forward transmission, the intensity of the light scattered into the forward angles was measured. Compared to a glass optical flat, the parallel sides of the hexagon scatter about a decade more light into the forward directions (0°–6°). These measurements indicate that the surface polish of the crystal is not interferometrically smooth.

The crystal was mounted on top of a small, 2-mm-diameter pedestal with glue as shown in Fig. 1a such that the scattered light is confined to the 2D or X–Y plane. Henceforth this orientation is called the 2D crystal. To completely describe the crystal position, a crystal orientation angle, β, is defined as illustrated in Fig 1a; $\beta = 0°$ when a crystal vertex is oriented into the incident light. The detector array is then oriented at $\phi = 0°$ or 180° to measure the 2D scattering profile.

b. *Fixed 2D NaF crystal*

Based on the geometric optics theory, the incident light is considered to be a tightly bunched bundle of

unidirectional rays incident on the crystal. These rays are reflected, transmitted, and refracted as they follow the physical laws of geometric optics at each air–NaF interface the ray encounter, as shown in Figs. 1c and 1d. In this manner, many rays may be traced through the crystal, and from the exit angle and intensity of each ray we can determine the theoretical scattering properties of the crystal, which can be plotted on a polar diagram as seen in Fig. 1b. Incident light approaches the crystal from the direction of the scattering angle of 180° and the hexagon figure in the center of the plot shows the crystal orientation angle β. Each dot shows the scattered angular direction of a theoretically predicted pencil of light, and its radial placement shows its intensity. The radial scale is logarithmic, the outermost ring has a value of 100, and the inner scale, at the hexagon outline, has a value of 0.1. Theoretical values less than or greater than these values are not shown since the experimental apparatus does not measure outside this range.

The forward intensity peaks near $\theta = 25°$, and symmetrically at 335°, are similar to the 22° halo produced by ice crystals and are caused by refraction through the 60° prism formed from two side faces. Also seen are the paths for the peak at 120° and the symmetrical peak at 240° that are due to the superposition of one external and one internal reflection, the paths for the peaks at $\theta \simeq 145°$ and $\theta \simeq 215°$ that are due to two internal reflections, and the peaks at $\theta \simeq 85°$ and $\theta \simeq 275°$ that are due to multiple internal reflections.

By properly orienting the 2D crystal with respect to the photodiode detector array, which has an angular sensing range of 90°, it is possible to experimentally measure the full 360° scattering pattern of the NaF crystal. Figure 2 shows scattering results for laser light polarized perpendicular and parallel to the scattering plane incident on the NaF hexagon oriented at $\beta = 5°$, 10°, and 25° (perpendicular) and $\beta = 0°$, 5°, and 10° (parallel). The experimental result for each separate scan was fitted to the theoretical data with a least squares method. Also shown, as small round dots, are the discrete theoretical predictions as calculated from ray tracing methods.

For both the parallel and perpendicular results there is more light scattered into the near forward ($\theta = 0°$–15°) directions than expected. This is caused by the surface imperfections, as discussed above, and also possibly by the finite width of the crystal vertices. In Fig. 2 (parallel), on the $\beta = 0°$ plot, this forward scattering is greater than that for the $\beta = 10°$ result. From other experimental results of this type, we have determined that the amount of light scattered into the near forward angles depends strongly on the crystal orientation angle. This effect is likely due to scattering by the small scratches and blemishes on the crystal that change their aspect to the incident light as the crystal is rotated about β. Though every effort was made to reduce reflections, light from the high intensity peaks is reflected off the

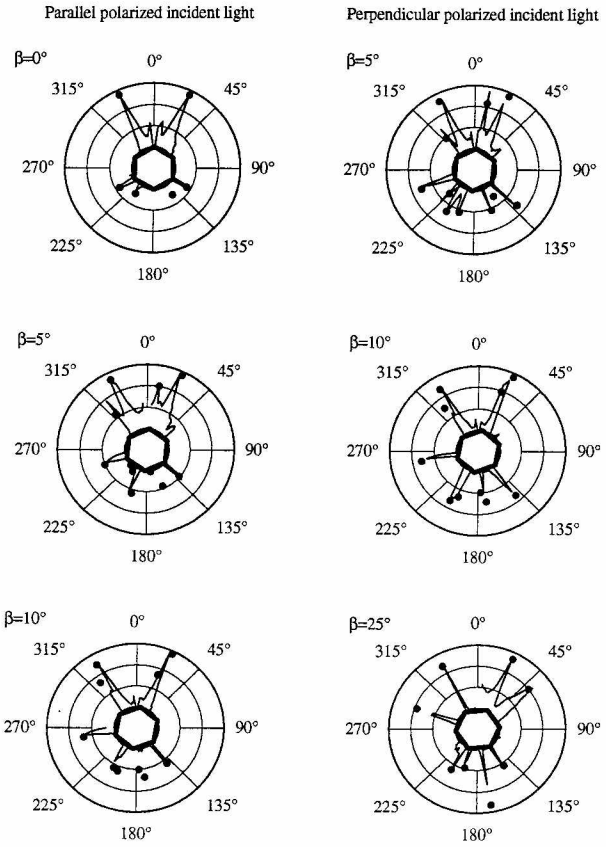

FIG. 2. Six polar plots of the experimental (lines) and theoretical (dots) results obtained for the large NaF hexagon oriented to produce a 2D scattering pattern at several different fixed orientation angles with incident light polarized perpendicular and parallel to the scattering plane. The radial scale is logarithmic, the outermost ring is 100, and the inner ring is 0.1.

experimental apparatus into detectors where light is not expected. This is seen as low intensity peaks, that is, near $\theta = 220°$ on the $\beta = 25°$ plot and near $\theta = 50°$ on the $\beta = 10°$ plot for the case of perpendicularly polarized light.

Since the detection of light by the detector array occurs at discrete points approximately 2.5° apart, we cannot accurately determine the exact angular locations of each of the scattered pencils of light. However, the experimentally measured peaks generally occur at the scattering angles predicted by the computer-generated ray tracing results.

From the results seen in Fig. 2, it is readily apparent that although the peaks produced by the NaF hexagon occur at the expected angular positions, the relative intensities do not correspond to the theoretically derived results. There are two reasons for this mismatch; the imperfections in the hexagonal scattering samples and the mismatch between the scattered peak and the photodiode detector angular position. In Fig. 2, on the $\beta = 5°$ plot (perpendicular), the experimental spot at $\theta = 130°$ is sharper than that seen at $\theta = 24°$. This indicates

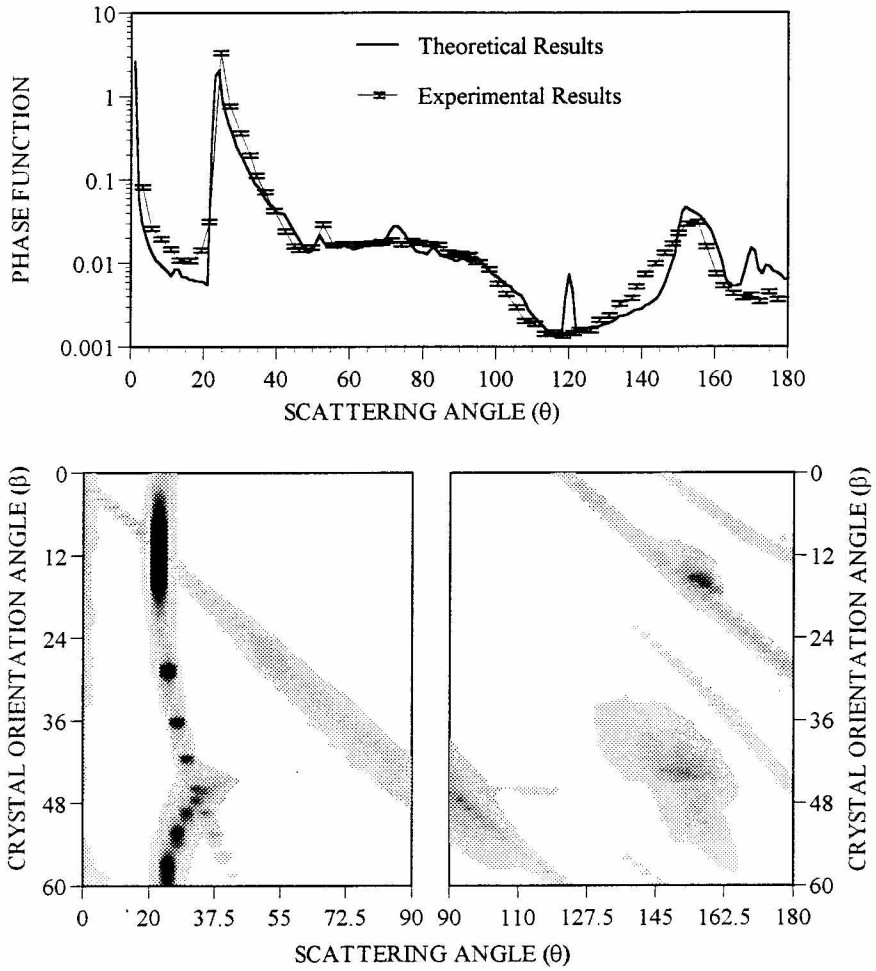

FIG. 3. Theoretical and experimental phase functions for helium neon laser light polarized parallel to the scattering plane incident on the 2D NaF. The lower contour plots show the experimental measurements used to produce the phase function. The intensity (z scale) of the contour plots is explained in the text.

that the light being produced at 24° is being spread out into a broader angular extent due to imperfections in the crystal. All other factors being equal, the broader beam of reflected light produces a smaller detector signal than a sharper, more concentrated pencil of light. Since the radial scales of Fig. 2 are logarithmic, it is realized that although there is spreading of each scattered pencil of light, these peaks approach the theoretically predicted very thin beam of light. The result is that a lower intensity peak that falls more directly onto a detector will produce a stronger photodiode signal than a larger peak that falls midway between two detectors. This may be the case in Fig. 2, the $\beta = 5°$ (parallel) case for the peaks at $\theta = 332°$ and 320°.

The integration of several measurements of the scattered light with the hexagon oriented in different positions reduces the effects of the discrete nature of the detectors and the scattered pencil of light. Also, the phase functions produced from this integration procedure represent the angular scattering properties of a cloud of randomly oriented 2D hexagons that are used to model the scattering properties of ice clouds in other computer algorithms (Takano and Liou 1989). To simulate random orientation of the 2D NaF crystal, a measurement of the scattered light is taken at each 0.2° increment between $\beta = 0°$ and 60°. The lower contour plot in Fig. 3 shows the results of one of these measurements with the incident light linearly polarized parallel to the scattering plane. Because the forward and reverse measurements are performed separately, these plots are divided into forward and reverse contour plots. On these contour plots, the Y ordinate is the crystal orientation angle and the X axes are the experimental photodiode detector angular locations. The contour or Z-axis scale for the forward direction is linear with white areas representing detector signals less than 0.01 and black areas representing signals greater than 1.0. The maximum detected signals in the forward direction

range up to eight, but due to the wide dynamic range of detected light signals, the higher signals are truncated to reveal scattering features at lower intensities. Because the dynamic range of detected light signals in the reverse direction is less than that in the forward direction, the reverse Z scale is not cut off: white contours are values less than 0.04 and black contours are detector signals greater than 14.

The pencil of light that is directly reflected off a hexagon side can be traced on the contour plot from $\beta = 0°$, $\theta \simeq 0°$ to $\beta \simeq 43°$, $\theta \simeq 90°$ and in the reverse direction from $\beta = 48°$, $\theta \simeq 90°$ to $\beta \simeq 60°$, $\theta \simeq 116°$ and then from $\beta = 0°$, $\theta \simeq 116°$ to $\beta \simeq 30°$, $\theta \simeq 180°$. The light that produces the 22° halo is also seen. Experimentally, light is not produced as narrow pencils of light but is spread out along the scattering direction by several degrees about the predicted point that is seen as wide contours rather than narrow points of light. The oscillating light and dark contours along some of the linear contours occur due to the narrow pencils of scattered light incident on the discrete detectors. The darker contours occur when there is coincidence between the scattered pencils of light and the photodiode detectors as the crystal is rotated through β.

The data seen in the lower contour plots of Fig. 3 are integrated across the β dimension to produce the phase function seen in the upper plot in the following manner:

$$I(\theta_i) = k \sum_{n=1}^{N} S(\theta_i, \beta_n), \tag{1}$$

where $I(\theta_i)$ is the integrated intensity at each photodiode detector angular location θ_i, k is a multiplicative constant used to fit the experimental results to the theoretical phase function, and $S(\theta_i, \beta_n)$ is the retrieved signal at the detector i and crystal orientation β_n. In this instance, β_n ranges from $\beta = 0°$ to $\beta = 60°$ in $\Delta\beta = 0.2°$, therefore $N = 300$. Integrated experimental phase functions are generated separately for the forward and reverse directions. These results are matched at $\theta \simeq 90°$ and then fitted to theoretical expectations by using a least squares fitting routine. Error bars of a constant 6% are placed on the experimental results, which reflects the accuracy of the photodiode detector array as discussed in Part I. Greater discrepancies between the theoretical results and experimental results are due to factors related to the sample geometric and optical characteristics.

Figure 4 shows the phase function results derived in the same manner as for Fig. 3 but with incident light polarized perpendicular to the scattering plane. The contour scales in this plot are as follows; in the forward direction, black regions are detector signals greater than 2.0 (maximum is about 3.5) and white areas are signals less than 0.01; in the reverse direction, black contours are retrieved detector signals of 14 and white areas are signals less than 0.1. Comparing both of the phase functions results to the theoretical results it is seen that there is more light scattered into the near-forward directions, $\theta \simeq 5°$–$20°$, and the intensity peaks at $\theta \simeq 24°$ and 150° are wider than predicted. We believe that these differences are due to the imperfect geometric and optical characteristics of the sample crystal. The noninterferometrically smooth surfaces of the NaF crystal greatly reduce the intensity of scattering features due to multiple internal reflections, which is why the expected peak at 120° is not seen and the experimental measurement is much lower than expected at $\theta > 165°$. These same anomalies are also produced by slightly distorted 3D ice columns in the theoretical calculations by Macke et al. (1996).

3. 3D NaF hexagon scattering measurements

a. Parry column

A series of naturally occurring arcs is believed to be caused by hexagonal columns oriented with two side faces parallel to the earth's surface as shown in Fig. 5a. Geometric ray tracing models predict that this Parry column orientation is consistent with the observed phenomena (Greenler 1980; Takano and Liou 1990). Seen in Fig. 5b are the modifications made to the sample holder in order to provide the corresponding experimental analog of the solar elevation angle, ϵ, and the random orientation of γ is provided by a motorized rotator.

Another NaF hexagonal crystal was manufactured in a manner similar to that described before. This crystal has a length of 9 mm and a width of 8 mm. Because this crystal is larger than that used in the 2D measurements, it is possible to polish the sides to a flatter and smoother finish. The end and side faces are parallel to within 1° as determined by measurement of the divergence of the beams of light reflected internally and externally from these surfaces. The radii of curvatures of the hexagon sides on this crystal are measured to be approximately 700 mm. Although the surfaces are not interferometrically smooth, measurements determined that these surfaces were optically flatter than the surfaces of the crystal used in the 2D measurements.

The procedure for measuring the scattering parameters were the same in both the forward and reverse directions, the only difference being the direction of the incident laser beam. To simulate randomness about the γ direction, γ is varied from 0° to 180° in $\Delta\gamma = 0.5°$ increments. The scattered light at each increment is measured by each photodiode detector at its respective scattering angle θ at the dome azimuthal position angle ϕ between 0° and 90° in $\Delta\phi = 0.5°$ increments. The crystal angle ϵ is kept constant at 30.8°.

The results of a ray tracing computer algorithm for this Parry column orientation with incident laser light polarized parallel to the horizontal (X–Y) plane are shown in Fig. 6. Results for light polarized perpendicular to the horizontal plane are similar. The results are

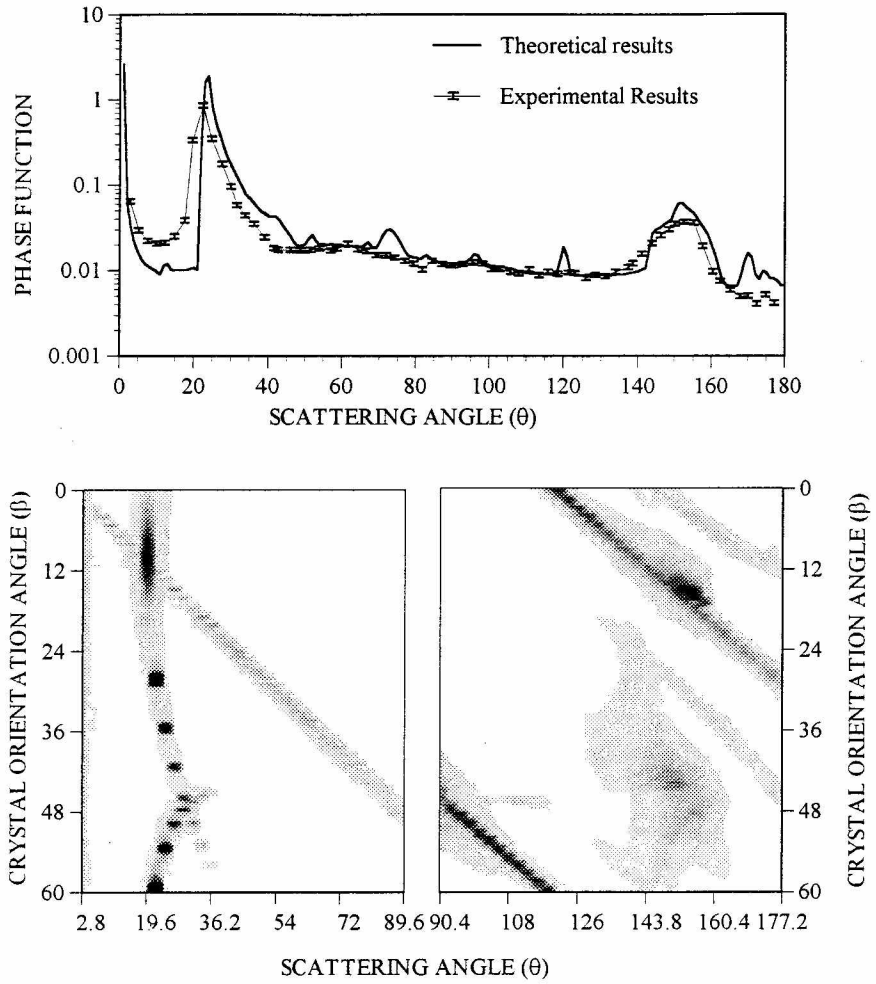

FIG. 4. The phase function experimentally derived in a manner similar to that seen in Fig. 3, except for these results the incident light is polarized perpendicular to the scattering plane.

determined at each 0.5° incremental azimuthal angle ϕ between 0° and 90° and, in the scattering direction, the results are determined in 1° bins about each photodiode detector location in the forward and the reverse directions. The tilt angle of $\epsilon = 30.8°$ was chosen to facilitate alignment as the crystal can be precisely aligned by aiming the pencil of light that is produced by reflection off the top hexagonal side when the incident light is directed for forward measurements, directly at the detector located at $\theta = 61.6°$ with the dome positioned at $\phi = 90°$.

The experimental apparatus can measure only the light scattered into one-quarter of the full 4π solid angle space about the sample by rotating the detector dome from $\phi = 0°$ to 180°. To measure the scattering information in the full 4π solid angle space about the sample, four separate scattering measurements were made with the sample properly oriented with respect to the incident light and the detector dome position. These measurement quadrants are labeled 1, 2, 3, and 4, as illustrated in Fig. 5c, and are also used to facilitate comparisons between theoretical expectations and the experimental results. A detailed description of the measurement method is given in Barkey (1997).

Figure 6 shows the intensities of the theoretically predicted scattering pattern at the scattering (θ) and azimuthal (ϕ) positions as seen on the experimental detector dome when viewed along the incident light in the forward direction. The scattering angle θ is the radial distance and the azimuthal angle is measured counterclockwise from the bottom. The left plots show the forward scattering or quadrant 1 and 4 results and the right plots show the reverse or quadrant 2 and 3 results. The intensity, or contour scale is as follows; for each quadrant, white represents those positions where the scattered light has intensities less than or equal to 0.001, black represents those locations with intensities greater than or equal to 0.01, and the gray areas correspond to linear delineations in between. The maximum intensity of these results is about 6 (at $\theta = 61.6°$ and $\phi = 90°$)

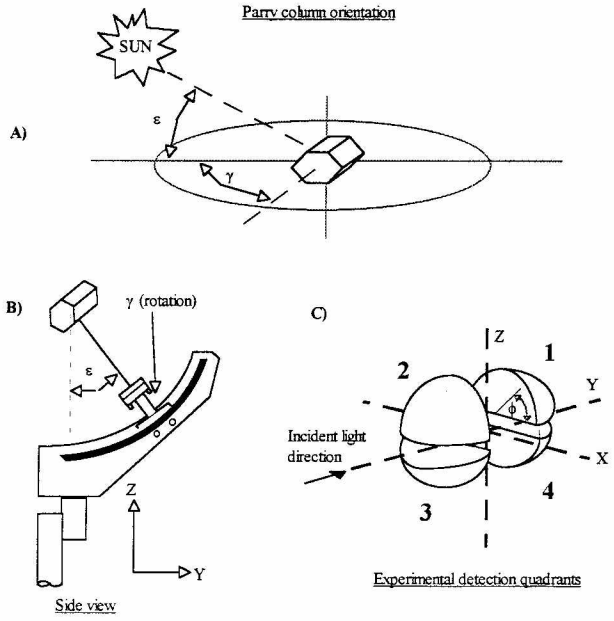

FIG. 5. (a) A diagram illustrating the Parry column orientation in the natural world. (b) The sample mount modified to provide the extra degree of freedom, ϵ, needed to reproduce the Parry column orientation in the laboratory. Here γ is provided by the motorized rotator. (c) The space about the scattering sample is separated into these four quadrants to facilitate comparisons between the theoretical expectations and the experimental results.

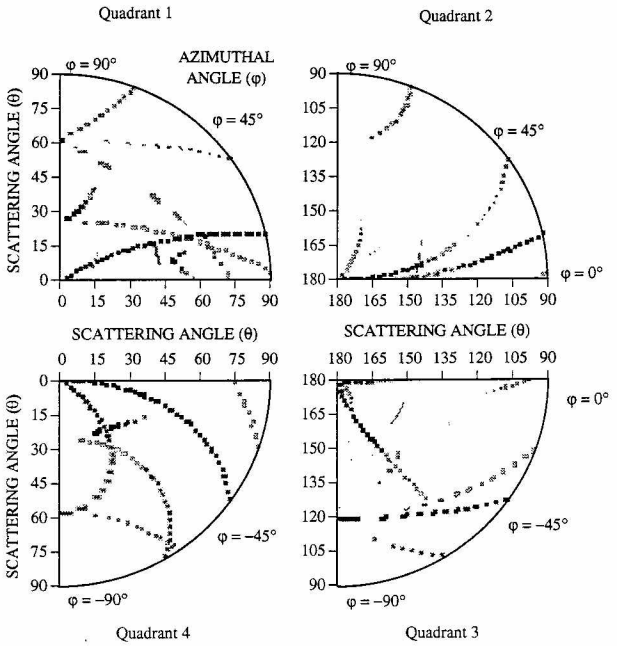

FIG. 6. Incident light polarized perpendicular to the scattering plane scattered by the NaF hexagonal column oriented as a Parry column at $\epsilon = 30.8°$ as determined via ray tracing methods. Details of this figure are given in the text.

but the scale has been truncated to reveal scattering features at lower intensities. The spots or intensity peaks that occur in a periodic manner along some of the features throughout Fig. 6 are due to coincidence between the discrete scattered light pencils and the discrete sensing areas of the photodiode detectors, which is also seen and discussed in the 2D results. The azimuthal range is limited from $-90°$ to $90°$ because of the scattering symmetry seen across the Y–Z plane.

The light pattern seen in Fig. 6 represents the light scattered by the NaF Parry column in a simulated random distribution about the γ orientation as expected for our experimental setup. The light patterns produced are a complex series of arcs produced by the many external and internal reflections and refractions of this crystal. It is possible to relate the arcs seen in Fig. 6 to their natural world counterparts, that is, the arc seen at $\theta \simeq 30°$ and $\phi \simeq 80°$ in quadrant 1 is the lower tangent arc. The terminology of these arcs is taken after Greenler (1980) and a more detailed description is given in Barkey (1997). The purpose of the experimental phase of this experiment is to see if these, and other scattering features, can be reproduced.

Shown in Fig. 7a are the experimentally measured scattering properties of the NaF hexagon integrated across the γ orientations between $\gamma = 0°$ and $180°$ at every $0.5°$ increment. This integration is a simple summation of the measured results produced as follows:

$$S(\theta_i, \phi_j; \epsilon) = \sum_{l=1}^{N} S(\theta_i, \phi_j; \epsilon, \gamma_l), \tag{2}$$

where $S(\theta_i, \phi_j; \epsilon, \gamma_l)$ is the photodiode detector signal at the detector scattering angle location θ_i, with the dome located at the incremental azimuthal position ϕ_j and the crystal tilted at $\epsilon = 30.8°$, and N is the number of different γ positions measured.

The format of this contour plot is similar to that shown in Fig. 6 and the incident light is polarized perpendicular to the horizontal plane. The linear contour, or Z axis, is truncated to reveal scattering events at lower intensities and since each plot is the result of a separate scan the contour intervals are not the same. For quadrant 1, white represents scattering regions where the integrated measured signals are less than 0.003, while black represents integrated signals greater than 4. The maximum integrated value in this quadrant is approximately 400. The extreme truncation in this quadrant is justified due to the relatively few positions with high-integrated signals. For quadrant 2 white represents integrated signals less than 1 and black represents positions where the integrated signals are greater than 10. For quadrant 3, white represents integrated signals less than 0.4 and black those greater than 4; in quadrant 4, white is less than 0.01 and black is greater than 1.

Almost all of the arcs calculated by theory are detected experimentally. However, the scattered peaks are broadened due to the noninterferometrically smooth surfaces of the NaF crystal as seen and discussed in the

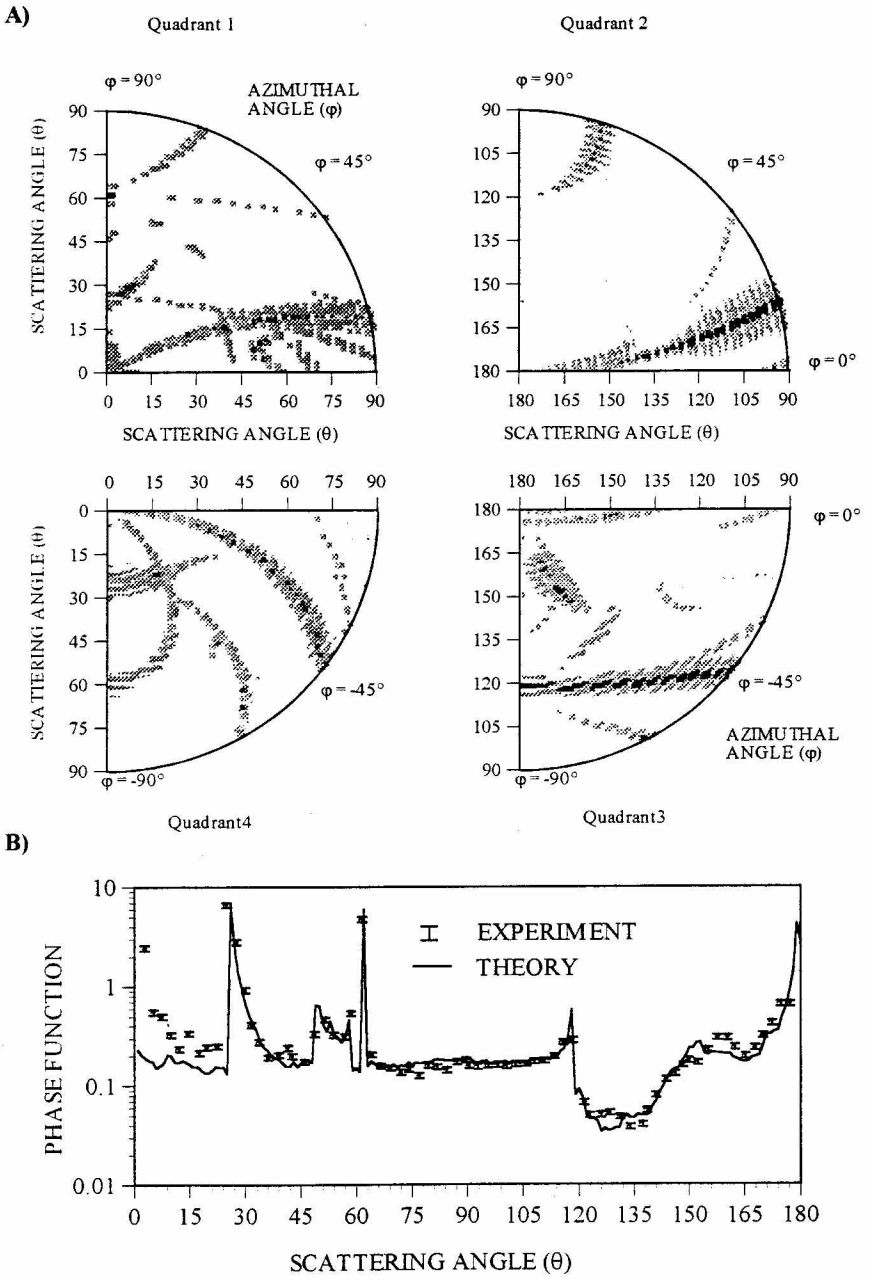

FIG. 7. The light scattered by the NaF hexagonal column oriented at $\epsilon = 60.8°$ and at each 1° increment from $\gamma = 0°$ to 180° as measured experimentally. Plotted are the detected signals integrated across the γ dimension as discussed in the text. (b) The phase functions produced by integrating the results in Figs. 6 and 7a across the azimuthal angle.

2D results. Several of the experimentally measured arcs are shifted slightly from the expected positions; that is, much of the heliac arc in quadrant 2 (at $\theta = 90°/\phi = 15°$ to $\theta = 135°/\phi = 0°$) is actually seen experimentally in quadrant 3 at $\theta = 135°/\phi = 0°$ to $\theta = 180°/\phi = 90°$. This is caused by both a slight misalignment of the crystal orientation in the apparatus and because of the deviation of the NaF sample from the perfect hexagonal geometry. The subanthelic arc in quadrant 2 at $\theta = 180°$, $\phi = 0°$ to $\theta = 150°$, $\phi = 90°$, and in quadrant 4 at $\theta = 90°$, $\phi = 55°$ to $\theta = 60°$, $\phi = 90°$, is not seen experimentally. This is because the noninterferometrically smooth surfaces of the NaF sample reduce the scattered light to nondetectable levels after multiple internal reflections. Finally, there are several arcs that are not predicted, for example, in quadrant 3 at $\theta = 120°$,

$\phi = -35°$ and in quadrant 4 at $\theta = 50°$, $\phi = -55°$. These are caused by spurious reflections in the experimental apparatus.

The experimental results are integrated across the azimuthal direction to produce the phase functions seen in Fig. 7b. Since the experimental measurement geometry is analogous to polar coordinates, this integration is a simple summation of the detected light signals as follows:

$$S(\theta_i;\ \epsilon) = \sum_{j=1}^{M} S(\theta_i,\ \phi_j;\ \epsilon), \tag{3}$$

where $S(\theta_i,\ \phi_j;\ \epsilon)$ are the detected signals integrated across the γ orientations as in Eq. (2) and M is the number of incremental azimuthal positions. This integration is performed separately for the results obtained from each quadrant and a least squares method is used to fit each of the four separate integrated results to the theoretically calculated and normalized results in each corresponding quadrant. These fitted results are then combined to produce the phase function seen in Fig. 7b. Also seen are the theoretical results plotted as a solid line, which are smoothed by determining the scattering results at 1° scattering increments, and they are normalized via

$$\int_{4\pi} \frac{1}{2}(P_{\parallel} + P_{\perp})\, d\Omega/4\pi = 1, \tag{4}$$

where $P_{\parallel}$ and $P_{\perp}$ are the phase functions for parallel and perpendicularly polarized incident light, respectively. Error bars of 6% have been placed on the experimental data points to reflect measurement uncertainty as discussed in Part I. Results for incident light polarized perpendicular to the horizontal plane are similar.

In the forward direction, the intensity peaks associated with refraction through the 60° ($\theta \simeq 25°$) and 90° ($\theta \simeq 47°$) prisms and the prominent peak due to external and internal reflection ($\theta \simeq 61°$) follow the theory fairly well. The experimental results in the far forward direction are higher than expected, which is probably due to diffraction around the small scratches and imperfections of the crystal, which are also seen and discussed in the 2D results. In analog measurements of the light scattered from actual ice crystals by Pluchino (1987) the light scattered into the forward direction are also higher than predicted. This may be an indication that real ice crystals have imperfections, causing more light to be scattered into the forward angles, which is a subject requiring more investigation.

In the reverse direction, the overall agreement between theory and experiment is quite good. The intensity peak at $\theta = 120°$ is present; however, it is reduced in intensity and has a wider scattering angle extent. This is presumed to be due again to the noninterferometric quality of the NaF model's surface, which produces scattered pencils of light with broadened angular extent instead of the narrow pencils of light predicted theoretically as seen in the 2D results. At $\theta \simeq 160°$ the experiment shows a peak with a higher intensity than is expected. Examination of Fig. 7a shows that this peak is due primarily to the light that forms the subanthelic arc in quadrant 3 ($\theta \simeq 170°$, $\phi \simeq 60°$). The subanthelic arc is due to light that enters an end face, internally reflects off a hexagon side, then the other end face, then another side face, and then exits via the same face it entered. Perhaps because the crystal is not geometrically perfect, this feature is diminished or redirected away from the expected direction.

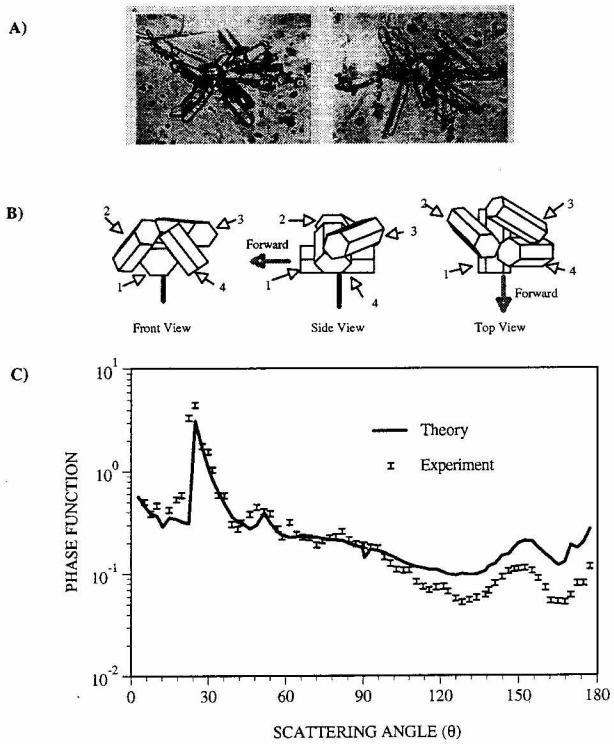

FIG. 8. (a) Examples of ice crystal aggregate collected in situ (Arnott et al. 1994). (b) The NaF aggregate constructed for this experiment. These diagrams are approximations and are not dimensionally accurate. (c) Theoretical and experimentally derived phase functions for an aggregate composed of NaF hexagonal crystals.

b. Aggregate

The spatial ice crystal form or aggregate is chosen because this crystal form is a major component of naturally occurring ice clouds (Heymsfield and Miloshevich 1993) and only recently has it been possible to model the light scattering properties of this shape using ray tracing methods (Takano and Liou 1995). In this experiment, the goal is to determine if there are any significant differences between the phase function produced experimentally and that produced theoretically. An aggregate collected in situ is shown in Fig. 8a. (Arnott et al. 1994). This crystal shape, which is represen-

tative of most aggregate shapes, shows several column crystals of various lengths connected at one point with an assortment of smaller crystals clustered in between the crystals. This is a complex shape and, at present, it is not possible to mimic with NaF hexagons; therefore we constructed a simplified version of this crystal.

Four small NaF hexagonal columns, approximately 5 mm in diameter and 10 mm long were assembled to produce an ice crystal aggregate as seen in Fig. 8b. To keep the attachment points on the crystals as small as possible, the NaF hexagons are attached by small glass fibers that are glued into small holes. Because these crystals are smaller than those previously constructed, they do not approach the geometric ideal nearly as well as the other crystals due to difficulties in the machining and polishing process. The crystal lengths vary between 10.0 and 10.1 $\pm$ 0.05 mm and the crystal diameters vary from 5.5 to 5.9 mm, and under visual inspection the hexagonal shape of the crystal faces appears asymmetrical. The degree of parallelism between opposite side faces and the end faces varies from 1° to 5° and the crystal optical properties are similar to those of the crystal described in the 2D measurement.

The goal of the experimental measurement of the scattering properties of the aggregate is to simulate the scattering properties of a single scattering cloud of randomly oriented aggregates as this is the assumed orientation of these crystals in nature. Also, if the assumption of randomness is valid in our experiment, then consideration of the symmetry conditions stipulated above can be ignored. The orientation specification for this crystal is based on the position of the lower crystal, labeled "1" in Fig. 8b. The orientation angles as described for the Parry column experiment in the previous section are used to describe the position of this reference crystal in the aggregate. To produce the experimental phase function, the crystal tilt ϵ is manually positioned and then the light scattered by the crystal is measured at the azimuthal positions of 0°–180° in 1° increments in both the forward and reverse directions at all of the 1° incremental γ orientations between 0° and 360°. This measurement at each ϵ orientation requires a sampling time of approximately two days; therefore only a few ϵ orientations are selected.

In Fig. 8c is seen the phase function as produced by the scattering results for the NaF aggregate integrated across the crystal orientation angles and the azimuthal angle. Here ϵ is oriented at 0°, $\pm$30°, and $\pm$60° and the incident light is unpolarized. Each measurement is integrated via the summation of measured detector signals as follows:

$$S(\theta_i, \epsilon_k) = \sum_{j=1}^{M} \sum_{l=1}^{L} (\theta_i, \phi_j; \epsilon_k, \gamma_l), \tag{5}$$

where M is the number of azimuthal (ϕ) orientations and L is the number of γ orientations. Each separate integrated result for each ϵ orientation is fitted to the theoretical results that are also seen in Fig. 8c, and then these adjusted results are averaged to produce the experimental phase function. The theoretical results are produced by integrating the scattering contributions across the full azimuthal dimension at the 1° incremental crystal orientations of γ = 0° to 360° and ϵ = 0° to 180°. In the derivation of the theoretical results randomness is simulated by determining the scattering results at every incremental crystal orientation of 1° between γ = 0° and 360° at every 1° incremental position of ϵ between 0° and 360°. The incident light for the theoretical results is unpolarized and they are normalized via

$$1 = \int_{4\pi} P(\Omega)\, d\Omega/4\pi, \tag{6}$$

where $P(\Omega)$ is the theoretically derived scattering results for the randomly oriented aggregate measured over the full 4π solid angle space.

There are several discrepancies seen between these two results. Most notable is that the experimental result is lower than the theory in the reverse direction. Although care was taken in constructing the NaF aggregate, there are still small glass fibers and glue at several points on the crystal that hold the columns together. The optical characteristics of these points are unknown. Since the experimental result is due to only a few ϵ orientations, this result is not the light scattered from a completely randomly oriented aggregate, as is calculated theoretically. This small number of ϵ orientations in the experimental measurement also produces the peaks that are seen at $\simeq$15° and 82°.

Otherwise, the main features seen in the theory are reproduced in the experiment, that is, the intensity peaks produced by refraction through both the 60° prism ($\theta \simeq 25°$) and the 90° prism ($\theta \simeq 47°$). The 90° prism peak is rounder than expected, which is because the 90° angles on the crystal are not all perfect right angles. In the reverse direction, the experiment shows a peak near θ = 152°, which is due to an internal reflection and there is evidence of a peak near $\theta \simeq 172°$, but it is less than the predicted error of the instrument.

c. *Rough surface*

One of the most difficult problems in ray tracing simulations is modeling the light scattering properties of an ice crystal with an irregular, or rough surface. Although there have been no studies concerned directly with the surface characteristics of atmospheric ice crystals, there is evidence that, for larger naturally occurring crystals, many of these surfaces are not the smooth, optically flat surfaces they are modeled as in the theoretical studies so far presented in this paper. Hallet and Mason (1958) showed that at certain temperatures and saturation levels, laboratory-generated ice crystals form "hopper" structures on their surfaces, that is, concav-

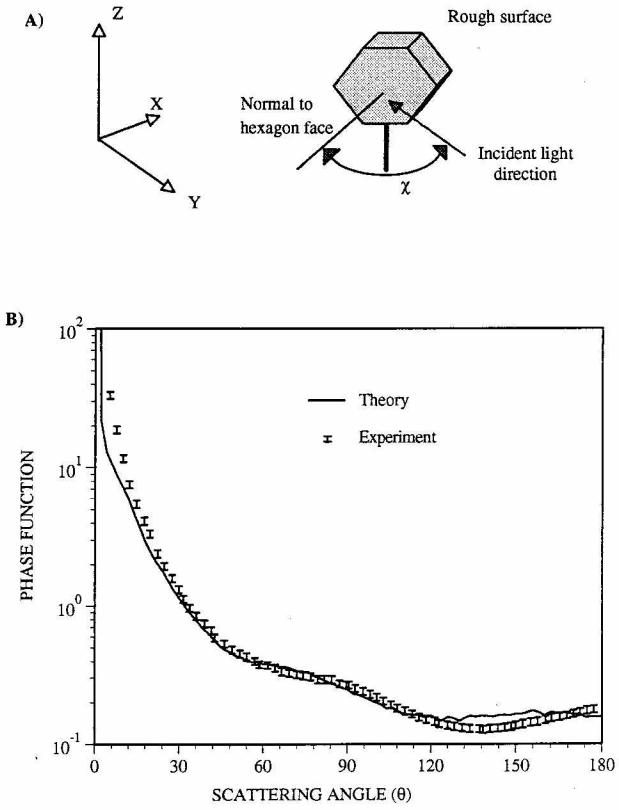

FIG. 9. Theoretical and experimental phase functions of the light scattered by a NaF hexagonal plate oriented as indicated and with surfaces roughened by 600 grit sandpaper.

ities formed by concentric steps in the ice crystal structure. Photographic evidence of naturally formed ice crystals by both Nakaya (1954) and Bentley and Humphreys (1931) show that the surfaces usually have intricate, hexagonally based patterns on their surfaces. Instead of trying to reproduce these features on an NaF hexagon, a random rough surface is used as an approximation of the surface roughness.

A NaF hexagonal crystal with a diameter of 5.2 mm and a thickness of 4.0 mm was polished such that its optical properties are similar to the surfaces previously described. To produce a rough surface, all eight sides were sanded lightly with 600 grit sandpaper. To the unaided eye, this crystal has a white, milky appearance and when examined closer, many small scratches were seen evenly distributed across the crystal surface. Scanning electron micrographs of this surface show that the scratches vary in size from 3 to 10 μm with many smaller features interspersed.

The crystal was mounted at the scattering center of the experimental apparatus with the perpendicular to the hexagonal faces and with two sides parallel to the horizontal X–Y plane as shown in Fig. 9a. The crystal was glued to a black sample post with a diameter of approximately 1 mm. The crystal was allowed to rotate about the vertical (Z) axis and the position of the crystal is specified by χ, which is defined to be the perpendicular to the two hexagonal faces; when χ is aligned with the incident laser beam direction, it is considered at $\chi = 0°$. In this configuration there are several symmetrical relationships that reduce the number of required scattering measurements. There is a two-fold symmetrical aspect above and below the horizontal plane, and for each crystal orientation χ between 0° and 180°, there is an analogous position between 180° and 360°. Therefore, a measurement in the forward and reverse directions of the light scattered into the azimuthal positions between 0° and 90° at all of the crystal orientations of χ between 0° and 180° will produce all of the scattering information necessary to produce a representative phase function for a crystal randomly oriented about χ.

The scattering properties for this crystal were calculated in the ray tracing manner similar to that described previously except for a provision that simulates surface roughness in a manner similar to Yang and Liou (1997) and Macke et al. (1996). At each point on the crystal surface at which a ray of light is incident, a random perturbation to the surface normal is determined. For a randomly oriented crystal, this perturbation simulates roughness by redirecting the light ray away from its normal path. The degree of roughness of the crystal surface is determined by the maximum amount of this perturbation. This scheme assumes that the sizes of the surface anomalies have scales consistent with this geometric optics assumption, and, due to the simplicity of this scheme, it is not possible to directly relate the characteristics of the NaF surface perturbations to the theoretical perturbations. Therefore, several different theoretical phase functions based on different levels of maximum perturbation angles were calculated and compared to the experimental results.

The phase function produced by this calculation is presented in Fig. 9b. The theoretical results are normalized such that it follows Eq. (6), and the limit of the perturbations to the normal is 36°. The experimental results, which are also seen in Fig. 9b, have been integrated as follows:

$$S(\theta_i) = \sum_{l=1}^{M} \sum_{k=1}^{N} S(\theta_i, \phi_k; \chi_l), \tag{7}$$

where $S(\theta_i, \phi_k; \chi_l)$ is the signal returned by each detector at θ_i and ϕ_k with the crystal positioned at one of the 2° incremental χ_l positions between 0° and 180°. These integrated experimental results, ignoring the forward scattering angles that are higher than expected, are fitted to the theoretical results using a least squares routine, and the error bars of 6% reflect the experimental uncertainty as described in Part I.

We see that from $\theta \simeq 25°$ to 180° the experimental results closely follow the predictions and at scattering angles less than 20°, the experimental results are higher than expected. The scanning electron photomicrographs

reveal that there are features on the roughened crystal surface with dimensions of about 0.5–1.0 μm. It may be possible that these features on the NaF crystal, which have dimensions smaller than or comparable to the size of the incident wavelength, are causing, via diffraction, more light to be scattered into these angles. The theoretical method assumes that all features on the crystal have dimensions larger than the incident wavelength. Between the scattering angles of about 120° and 160°, the experiment is lower than predicted, and in the far reverse direction the experimental result increases above the prediction. This may be caused because of the differences between the modeled roughness and the actual surface configuration. This same scattering feature is seen in the results of Peltoniemi et al. (1989) for spheres with light to medium roughness.

4. Summary and conclusions

Several measurements of the angular scattering pattern for a machined and polished NaF hexagonal column crystal oriented such that its scattering profile is confined to a 2D plane have been presented. Because of the design of this experiment, direct comparison between these results to those derived via theoretical ray tracing results are possible. The comparison of a fixed crystal orientation showed that, within the angular resolution of this experiment, the theoretical calculations place the scattered pencils of light at the correct positions for those pencils of light detected by this experiment. Several 2D scans of the crystal have been integrated to produce a phase function that compares very well to similar theoretically derived phase functions. The differences can be attributed to imperfections of the surfaces and the imperfect geometry of the NaF hexagonal crystal. Some of the optical effects of these imperfections have been measured to provide verification of this hypothesis.

The scattering pattern from the Parry column was studied in detail. Several experimental methods of measuring the light scattered into the 3D space by this crystal have been devised, including methods with which to simulate random orientations of this crystal, methods to measure the light scattered into the full 3D space about this crystal, and a method with which to integrate the resulting measurements into a phase function for comparison to theoretically derived results. The comparison of the experimentally measured and theoretically derived scattering pattern from the Parry column orientation showed that except for factors associated with imperfections in the NaF hexagonal crystal, the two results compare favorably within the experimental error associated with this apparatus.

Four small NaF hexagonal crystals were assembled to approximate a naturally occurring aggregate ice crystal and the phase functions derived from this crystal were compared to those derived via ray tracing methods. Complete randomness of the crystal orientation is simulated in the theoretical calculations, but due to physical and time constraints, complete randomness of the NaF aggregate crystal is difficult to achieve experimentally. The experimental results are higher in the forward direction and lower in the reverse. Several reasons for this theoretical to experimental result mismatch are postulated, including the geometric and surface imperfections of the NaF crystals and the unknown optical effect of the glue used to assemble the aggregate model.

The light scattered from an NaF hexagonal plate crystal with rough surfaces is compared to theoretically derived results that mimic this case. In the reverse direction, the two results agree within the error limits of the apparatus, but in the forward direction, the experimental results are higher than expected. This is most likely caused by features on the roughened crystal surface that have sizes comparable to the wavelength of the incident light diffracting light away from the forward direction.

In conclusion, within the experimental measurement uncertainties, the geometric ray tracing approach is an excellent method to determine the scattering characteristics of hexagonal ice crystals in the domain of geometric optics.

Acknowledgments. This research was supported by NSF Grant ATM-93-15251. Some of the theoretical calculations in this paper have been made by Dr. P. Yang. W. Wingert of the University of Utah crystal growth lab helped with crystal preparation.

REFERENCES

Arnott, W. P., Y. Y. Dong, J. Hallet, and M. Poellot, 1994: Role of small ice crystals in radiative properties of cirrus: A case study, FIRE II, November 22, 1991. *J. Geophys. Res.*, **99,** 1371–1381.

Barkey, B., 1997: An analog light scattering experiment of hexagonal ice-like particles. Ph.D. thesis, University of Utah, 161 pp.

———, K. N. Liou, W. Gellerman, and P. Sokolsky, 1999: An analog light scattering experiment of hexagonal icelike particle. Part I: Experimental apparatus and test measurements. *J. Atmos. Sci.*, **56,** 605–612.

Bentley, W. A., and W. J. Humphreys, 1931: *Snow Crystals.* McGraw Hill, 277 pp.

Greenler, R., 1980: *Rainbows, Halos and Glories.* Cambridge University Press, 195 pp.

Hallet, J., and B. Mason, 1958: The influence of temperature and supersaturation on the habit of ice crystals grown from the vapour. *Proc. Roy. Soc. London A.*, **247,** 440–453.

Heymsfield, A. J., and L. M. Miloshevich, 1993: Overview of microphysics and state parameter measurements from FIRE II. *Proc. Conf. on FIRE Cirrus Research,* Breckenridge, CO, NASA, 1–4.

Macke, A., J. Mueller, and E. Raschke, 1996: Single-scattering properties of atmospheric ice crystals. *J. Atmos. Sci.*, **53,** 2813–2825.

Nakaya, U., 1954: *Snow Crystal: Natural and Artificial.* Harvard University Press, 510 pp.

Peltoniemi, J. I., K. Lumme, K. Muinonen, and W. M. Irvine, 1989: Scattering of light by stochastically rough particles. *Appl. Opt.*, **28,** 4088–4095.

Pluchino, A., 1987: Scattering photometer for measuring single ice crystals and evaporation and condensation rates of liquid droplets. *J. Opt. Soc. Amer. A,* **4,** 614–620.

Sassen, K., and K. N. Liou, 1979: Scattering of polarized laser light by water droplet, mixed phase and ice crystal cloud. Part I: Angular scattering patterns. *J. Atmos. Sci.,* **36,** 852–861.

Takano, Y., and K. N. Liou, 1989: Solar radiative transfer in cirrus clouds. Part I: Single-scattering and optical properties of hexagonal ice crystals. *J. Atmos. Sci.,* **46,** 3–19.

——, and ——, 1990: Halo phenomena modified by multiple scattering. *J. Opt. Soc. Amer. A,* **7,** 885–889.

——, and ——, 1995: Radiative transfer in cirrus clouds. Part III: Light scattering by irregular ice crystals. *J. Atmos. Sci.,* **52,** 818–837.

Yang, P., and K. N. Liou, 1997: Light scattering by ice crystals of complex shapes. *Proc. Ninth Conf. on Atmospheric Radiation,* Long Beach, CA, Amer. Meteor. Soc., 373–377.